X-ray Micro-Computed Tomography of Polymer Electrolyte Fuel Cells: What is the Representative Elementary Area?

View the article online for updates and enhancements.

X-ray Micro-Computed Tomography of Polymer Electrolyte Fuel Cells: What is the Representative Elementary Area?

Jennifer Hack,[1,2] Pablo A. García-Salaberri,[3,z] Matthew D. R. Kok,[1] Rhodri Jervis,[1] Paul R. Shearing,[1,*] Nigel Brandon,[2] and Dan J. L. Brett[1,z]

[1]*Electrochemical Innovation Lab, Department of Chemical Engineering, University College London, London, WC1E 7JE, United Kingdom*
[2]*Department of Earth Sciences and Engineering, Royal School of Mines, Imperial College London, London SW7 2BP, United Kingdom*
[3]*Departamento de Ingeniería Térmica y de Fluidos, Universidad Carlos III de Madrid, Leganés 28911, Spain*

With the growing use of X-ray computed tomography (X-ray CT) datasets for modelling of transport properties, comes the need to define the representative elementary volume (REV) if considering three dimensions or the representative elementary area (REA) if considering two dimensions. The resolution used for imaging must be suited to the features of interest in the sample and the region-of-interest must be sufficiently large to capture key information. Polymer electrolyte fuel cells have a hierarchical structure, with materials spanning multiple length scales. The work presented here examines the nature of the REA throughout a 25 cm^2 membrane electrode assembly (MEA), focusing specifically on the micron length scale. Studies were carried out to investigate key structural (volume fraction, layer and penetration thickness, pore diameters) and transport (effective diffusivity) properties. Furthermore, the limiting current density of the nine regions was modelled. Stochastic heterogeneity throughout the sample results in local variations throughout. Finally, effects of resolution were probed by imaging using a range of optical magnifications (4× and 20×). The correlated and competing effects of voxel resolution and sampling size were found to cause difficulties where loss of clarity in the boundaries between phases occurs with larger imaging volumes.

Supplementary material for this article is available online

The use of X-ray computed tomography (X-ray CT) for three-dimensional imaging has many advantages including the ability to carry out non-destructive imaging of samples and the flexibility in resolution capabilities.[1–3] The rising availability of laboratory-based X-ray sources has led to a growth in the use of X-ray CT in many fields, including electrochemistry.[4–8] Electrochemical energy conversion and storage devices, such as fuel cells and batteries, contain electrodes that are typically tens or hundreds of cm^2 in size. However, the key materials making up the electrode microstructure (such as the fibres of the gas diffusion layer or the secondary active particles in Li-ion battery electrodes) are on the order of microns in size. This presents a difficulty in imaging such devices and there is an inherent trade-off between resolution and imaging volume; resolving the small features of interest in electrochemical devices restricts the volume that can be imaged.

Efficient operation of polymer electrolyte fuel cells (PEFCs) relies on material properties that span multiple length scales, from nanometres to centimetres,[9] which makes selection of the imaging parameters essential for targeting the feature of interest. The fuel cell membrane electrode assembly (MEA) is comprised of two gas diffusion electrodes (GDEs), which sandwich a proton-conducting polymeric membrane. The GDE comprises a layered structure with hierarchical porosity from the gas diffusion layer (GDL, woven carbon fibres of around 10 μm in diameter), the microporous layer (MPL, porous carbon with particle diameter around 40 nm) and the catalyst layer (CL, platinum nanoparticles of diameter around 3–8 nm supported on carbon particles of ∼30 nm).

In order to provide a range of magnifications, the detectors in CT systems can be coupled with scintillators and optical magnification, allowing higher resolutions to be achieved than with simple geometric magnification of a conical beam profile.[3,10,11] At the "micron" length scale, the GDL is the only layer of the MEA with resolvable features, though properties of the MPL and CL, such as

overall thickness or extent of cracking, can be resolved using X-ray micro-CT. There has been a wide range of studies probing the morphology and microstructure of PEFC materials.[12–14] Furthermore, the field of image-based modelling has been growing; using real 3D images of PEFC samples to model various transport processes.[15–17] The transport of multiple species, namely protons, electrons, gas and water, throughout the PEFC are critical for achieving optimal cell performance, and understanding these processes allows for more informed materials design and cell engineering.

With the broad span of length scales present in the MEA, questions arise as to the representative nature of a small volume that has been imaged from a much larger sample. Use of the representative elementary volume (REV) or representative elementary area (REA) is a commonly employed method for finding the minimum volume or area of a sample that is representative of the entire sample.[18,19] The REV and REA are particularly important for modelling studies across all length scales, since the transport properties investigated should represent the real-world conditions as closely as possible. REV analyses of the nanoscale pores in the CLs have been carried out,[20,21] as well as analysis of the properties of GDLs at the microscale[18] and investigation of the REV of different GDLs under compression.[22] However, to the authors' knowledge, the work discussed here is the first example of an investigation into the REA of an entire GDE at the micron length scale, which includes both the MPL and the CL. The REA is of interest here, because the full thickness of the GDE is used in all cases. This study explores the various morphological and transport properties throughout multiple regions of a 25 cm^2 GDE.

Experimental and Methodology

Materials and sample preparation.—Gas diffusion electrodes (GDEs) were obtained from HyPlat (HyPlat, South Africa), with a platinum loading of 0.4 mg$_{Pt}$ cm^{-2} and a GORE-SELECT M8 30.25 membrane (Gore, USA) was sandwiched between the GDEs. The electrodes employ a Freudenberg H23C9 carbon paper with MPL

(Freudenberg, Germany), which contains a felt-like GDL paper that has had hydrophobic treatment to facilitate water management in the electrode. An MEA with an area of 25 cm^2 was assembled by hot-pressing at 400 psi for 3 min at a temperature of 150 °C, in line with the membrane manufacturer's recommendations. Whilst this study focuses on only one of the two GDEs in the MEA, hot-pressing of a full MEA was still carried out in order to represent as closely as possible an MEA that would be used in an operating fuel cell.

After hot pressing, the electrode surface area was divided into a 3 × 3 grid (Fig. 1a) and a cylindrical sample with a diameter of 2 mm was taken from the centre of each region using a biopsy punch (Miltex Instruments, USA). Each sample was then mounted onto the head of a pin and affixed with double sided tape for imaging, with a total of nine regions of interest (ROIs) imaged.

X–ray computed tomography and image post-processing.—A Zeiss XRadia Versa 520 (Zeiss, USA) was used for scanning the samples. Various optics were employed for the different scans, but a source voltage of 80 kV and power of 7 W were used for each scan. Each of the nine MEA segments were scanned using the 4× optic, with a field-of-view (FOV) of 2 mm × 2 mm, such that the entire sample fitted inside the FOV. Scans were carried out with 1601 projections and an exposure time of 2 s per radiograph. The source and detector were positioned at an identical distance from the sample each time to afford the same voxel size and imaging conditions. A filtered back projection (FBP) reconstruction algorithm was used to generate the 3D volume, which resulted in datasets with voxel size of 1.16 μm.

For the central sample (region 5), an additional internal scan using a 20× optic was carried out on the central region of the 2 mm punch, with a FOV of 0.7 mm × 0.7 mm. 3201 projections were acquired with an exposure time of 13 s per radiograph and after reconstruction with an FBP algorithm, the dataset had a voxel size of 0.36 μm.

After scanning, an internal section of the dataset was isolated (see Fig. S1 available online at stacks.iop.org/JES/167/013545/mmedia),

with the dimensions of the bounding box fixed to be identical for each sample, with the $x \times y \times z$ dimensions being shown in term of both microns and number of voxels in Table I, where the $x \times y \times z$ axes are indicated in Fig. 1b. Images were then segmented into their constituent phases, namely GDL (carbon fibres), MPL and CL using the 3D visualisation and data processing software Avizo (Thermo Fisher Scientific, USA). Segmentation is the process by which every grayscale voxel associated with each phase is assigned a "label." Thus, the dataset is converted from a 16-bit image with a grayscale histogram to an 8-bit label field, with discreet values for each phase. Since the MEA is symmetrical around the membrane, only one GDE was segmented for the study. A range of segmentation techniques were used, including thresholding and manual segmentation with local adaptive thresholding techniques, and have been described fully elsewhere.[10] At the resolution of interest here, the nano-porosity of the CL and MPL cannot be resolved, so these phases are treated as solid, bulk structures. For modelling studies, bulk properties for porosity or diffusivity are taken from the literature and assigned to these phases, as is discussed in more detail in the following section.

Modelling and analysis of sample properties.—Once each sample had been segmented, a variety of metrics of interest were analysed. The metrics of interest were categorised into:

(a) Microstructural qualities: volume fraction; phase and penetration thickness; and tortuosity factor and pore size distribution of gas diffusion layers
(b) Transport properties: effective diffusivity
(c) Electrochemical properties: limiting current density

Volume fractions of each phase were calculated using the "*Volume Fraction*" module in Avizo, by calculating the fraction of voxels assigned to each phase as a percentage of the total number of voxels in the volume. The average layer thickness of each phase was
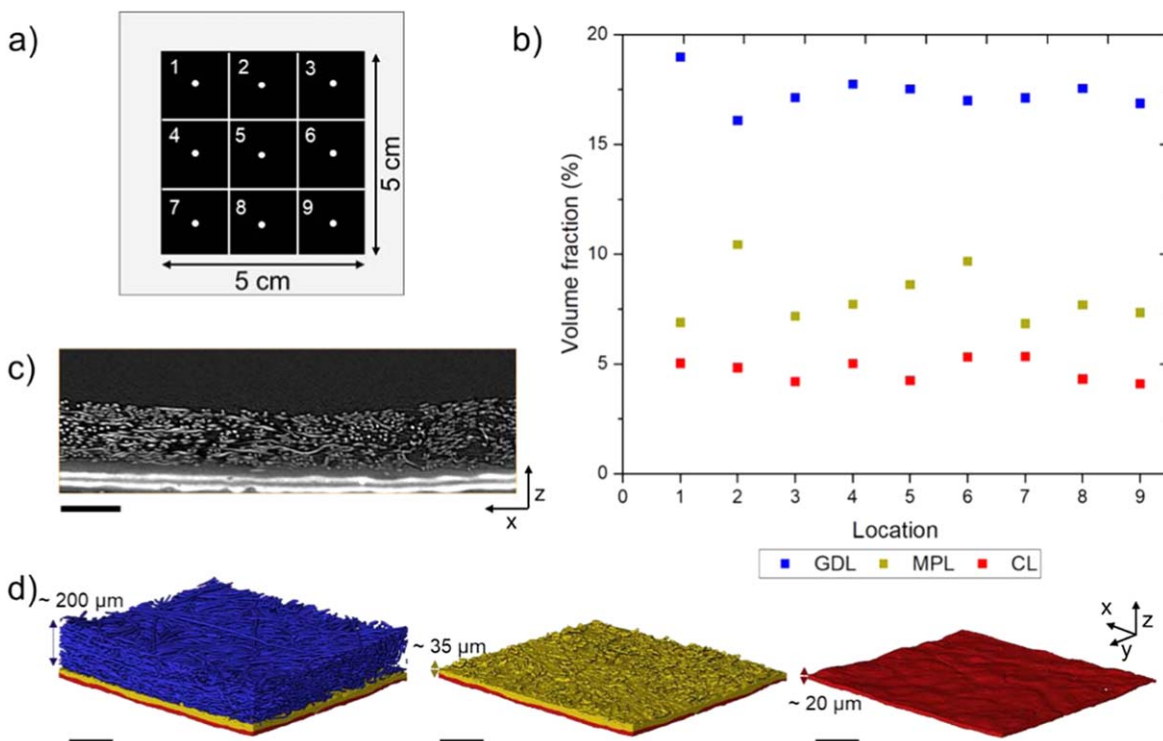
Figure 1. (a) Schematic of the nine ROIs that were scanned. Electrode area is 25 cm^2 and circle diameter of each punch is 2 mm, (b) the volume fraction of each phase in an identical 3D box for each region, (c) grayscale orthoslice from region 5 in the xz plane and (d) example volume rendering of the three segmented phases, GDL (blue), MPL (yellow) and CL (red), from region 5. The arrows in (d) represent the approximate thickness of each layer, with the GDL being around 200 μm thick, the MPL being around 35 μm and the CL being around 20 μm thick. Scalebars in (b) and (c) represent 200 μm.

Table I. Information about the scan parameters and features of the reconstructed datasets, including voxel size and bounding box for each sample.

Optic	FOV/mm × mm	Exposure time/s	Voxel size/μm	Bounding box ($x \times y \times z$) dimensions/μm	Bounding box ($x \times y \times z$) voxel dimensions/-
4×	2 × 2	2	1.16	1200 × 1200 × 400	1034 × 1034 × 345
20×	0.7 × 0.7	13	0.36	450 × 450 × 400	1250 × 1250 × 1111

calculated by determining the maximum and minimum z-position of each phase at every (x,y) position in the image stack, followed by taking the average across every (x,y) position of the maximum z-position minus the minimum z-position (where x, y and z axes are defined as shown in Fig. 1d). The penetration depth of the MPL into the GDL was then extracted by calculating the average of the maximum MPL z-position minus the minimum GDL z-position. Points where the minimum GDL voxel fell above the maximum MPL voxel, *i.e* the value for penetration depth was negative, were not included in the analysis, since a negative value indicates that there is no penetration of the MPL into the GDL. The penetration depth for MPL-GDL was also calculated as a function of the GDL thickness by division of penetration depth by the total thickness of the GDL.

In order to investigate key metrics of interest surrounding the GDL, namely tortuosity factor and pore size distribution, a 100 μm thick volume (dimensions 1200 μm × 1200 μm × 100 μm) was extracted from the GDL phase of each region, which ensured that the GDL entirely filled the bounding box (as shown in Fig. 2a). The resulting volume, which now consisted of only two phases ("GDL" and "pore") was then used for tortuosity and pore size distribution calculations. TauFactor,[23] an open-source MATLAB application, was used for the calculation of the tortuosity factor of the GDL. The application determines the tortuosity factor of the phase of interest, in this case the pore phase, by solving the diffusion equation for that phase. The pore size distribution in the GDL was calculated using PoreSpy, an open-source tool available in Python for analysing the pore structures in 3D datasets,[24] which applies a local thickness method that uses a fast Fourier convolution to calculate the local thickness of the pore phase at each region. Thus, metrics concerning the pores in a 3D dataset, such as pore diameter or pore size distribution can be obtained. A pore size distribution is then calculated on the processed dataset.

To include the effect of the MPL on the transport properties, effective diffusivity was calculated using the finite-volume-based code ANSYS Fluent (ANSYS, Inc., USA), which employs computational fluid dynamics (CFD) methods for modelling of the physical properties of a dataset. The simulation campaign included both full-thickness GDL samples with and without the MPL to assess the relative impact of the MPL on the effective diffusivity. The square-shaped samples were 1200 μm wide. In the thickness direction (z-direction), the unstructured meshing capabilities of ANSYS Fluent where used to accommodate the irregular surfaces of the material and crop the desired computational domains from the raw samples. The GDL-only domains were cropped at the average maximum and minimum z-coordinate of the GDL solid phase. Similarly, the top surface of the GDL + MPL domains was set at the average maximum z-coordinate of the GDL solid phase, while the bottom surface of the domain was set at the interface between the MPL and the CL. A concentration differential was prescribed in the through-plane direction, using a no flux boundary condition at the side walls of the domain and the solid-phase (i.e. fibres) surface. Bulk diffusivity was set in the void space of the GDL, treating the MPL as an effective porous medium with an effective diffusivity $D_{mpl}^{eff}/D^{bulk} = 0.15$.[25–27] The normalised effective diffusivity was calculated as

$$f = \frac{D^{eff}}{D^{bulk}} = \frac{\left(\iiint_V j dV\right)/V}{D^{bulk} \Delta C/L} \quad [1]$$

where V is the volume of the sample, ΔC is the prescribed concentration differential, L is the thickness of the sample and j is the local diffusive flux in the direction of interest.

The limiting current density was investigated for two cases: (1) considering the GDL only (without MPL) and (2) considering both the GDL + MPL. The main assumptions used in the calculations are as follows:

1. The reactant stoichiometry is infinitely high, so the oxygen concentration in the channel, $C_{O_2}^{ch}$, is approximately constant along the channel.
2. The dry effective diffusivity of the MPL phase ($D_{mpl}^{eff}/D^{bulk} = 0.15$) and the average water saturation are the same in all the samples.
3. The relative effect of water blockage on gas diffusion depends only on average saturation. The average saturation decreases when an MPL is added.
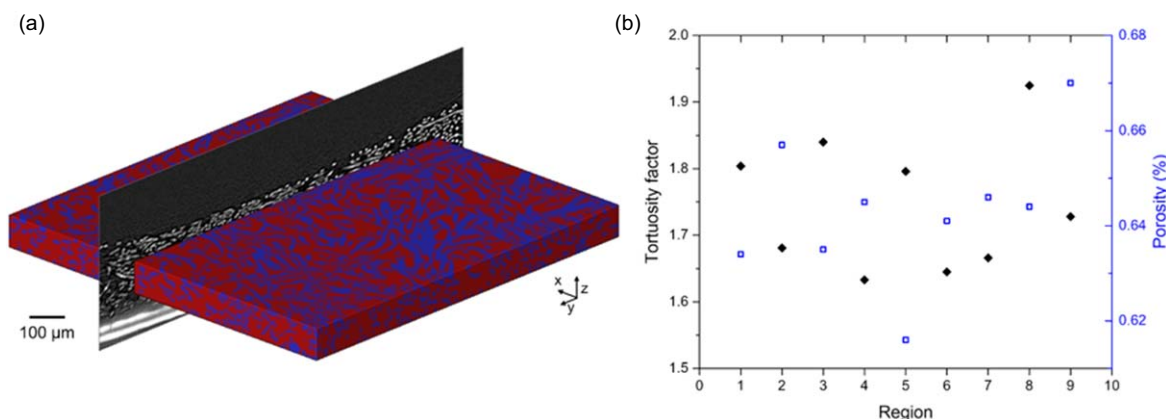
Figure 2. (a) Volume rendering of the fibre subvolume for region 5, with fibre (blue) and pore (red) and an orthoslice to highlight the region of the subvolume that has been extracted, (b) the tortuosity factor for each location, 1–9, (black left axis, black closed diamonds) is shown with corresponding porosity of each region (blue right axis, blue open squares).

Table II. Thickness of the three layers (GDL, MPL and CL), as well as the interpenetration thickness of the MPL into the GDL, with numbers in brackets representing the percentage of interpenetration as a function of GDL thickness.

Region	Thickness (GDL)/μm	Thickness (MPL)/μm	Thickness (CL)/μm	Interpenetration thickness, GDL-MPL/μm
1	181.35	29.12	19.11	17.85 (9.84%)[a]
2	157.17	44.36	18.24	17.55 (11.17%)
3	166.99	31.77	15.66	16.08 (9.63%)
4	171.83	30.13	18.92	12.91 (7.51%)
5	165.47	35.42	15.91	15.41 (9.31%)
6	160.12	39.14	20.13	14.00 (8.74%)
7	172.94	28.27	21.14	10.57 (6.11%)
8	180.55	31.16	16.15	14.27 (7.90%)
9	171.63	28.90	15.29	8.88 (5.17%)

a) Numbers in brackets correspond to the interpenetration thickness as a function of the GDL thickness.

Under these conditions, the limiting current density is given by the following expression:

$$I_{lim} = \frac{4F}{R_{O_2}} C_{O_2}^{ch} \qquad [2]$$

where F is the Faraday constant and R_{O_2} is the across-the-channel oxygen mass transport resistance between the channel and the catalyst layer. The oxygen concentration in the channel can be determined as

$$c_{O_2}^{ch} = 0.21(c_g - c_{H_2O}); \; c_g = \frac{p_g}{RT}; \; c_{H_2O} = \frac{RH\, p_{H_2O}^{sat}}{RT} \qquad [3]$$

where p_g, T and RH are the operating pressure, temperature and relative humidity, respectively, and $p_{H_2O}^{sat}$ is the saturation pressure of water; $\log_{10}(p_{H_2O}^{sat}) = -2.18 + 2.95 \times 10^{-2}(T - 273.15) - 9.18 \times 10^{-5}(T - 273.15)^2 + 1.44 \times 10^{-7}(T - 273.15)^3$ atm.[28]

The (diffusive) oxygen mass transport resistance is given by

$$R_{O_2} = \frac{L_{gdl(+mpl)}}{D_{gdl(+mpl)}^{eff,wet}} \qquad [4]$$

where $L_{gdl(+mpl)}$ is the sample thickness including or not including the MPL (see Supplementary Information), and $D_{gdl(+mpl)}^{eff}$ is the effective diffusivity of the GDL-only or GDL-MPL composite layer under wet conditions.

The effective diffusivity can be expressed as

$$D_{gdl(+mpl)}^{eff,wet} = D^{bulk} f(\varepsilon) g(s) \qquad [5]$$

where $D_{O_2}^{bulk} = 2.65 \times 10^{-5}(T/333)^{1.5}(10^5/p_g)$ is the bulk oxygen diffusivity,[29] $f(\varepsilon) = D_{gdl(+mpl)}^{eff,dry}/D^{bulk}$ is the normalised dry effective diffusivity computed in each sample (See Fig. 4), and $g(s) = D_{gdl(+mpl)}^{eff,wet}/D_{gdl(+mpl)}^{eff,dry}$ is the relative effective diffusivity, which accounts for the relative effect of water blockage on oxygen diffusion. Here, we considered a power-law of the form $g(s) = (1 - s_{avg})^3$, assuming a representative average saturation $s_{avg} = 0.25$ for the MPL-coated GDL and $s_{avg} = 0.4$ for the GDL substrate alone.[15,30] This agrees with previous works,[31–33] which showed that the addition of an MPL leads to better performance mainly due to an improvement in water management. The uniformity of the limiting current density distribution in the two cases (GDL only and GDL + MPL) was measured using a homogeneity factor (HF),

$$HF = 1 - \frac{\sigma}{\bar{I}_{lim}} \qquad [6]$$

where σ is the standard deviation and $\bar{I}_{lim}$ is the mean limiting current density of the nine regions.

Using these metrics, the studies carried out can be summarised into three separate investigations:

(a) Investigation 1: Comparison of the nine ROIs scanned with 4× optics.

(b) Investigation 2: Comparison of the central region scanned at 4× and 20× magnification.

(c) Investigation 3: Incremental growth of an ROI scanned at 4× and at 20× and analysis of spatial variations.

Results and Discussion

Investigation 1: comparison of nine ROIs.— *Volume fraction of phases.*—A schematic of the nine ROIs scanned in this investigation is shown in Fig. 1a. Following segmentation of the nine regions (Fig. 1d), the 3D volume fraction for each phase was calculated for the entire ROI (Fig. 1d). The values for the total volume fraction of carbon fibres in the samples ranged from 16.1% − 19.0%, the MPL showed a slightly larger range, with values between 6.9% − 12.5% and the CL ranged from 4.1% − 5.2%. Considering that the *xy* dimensions of each ROI are 1.2 mm × 1.2 mm, the area of a single region corresponds to only 0.06% of the total MEA area that was hot-pressed (with an area of 50 mm × 50 mm). Thus, the variation of values reported throughout the nine regions of the sample is low, when considering the difference in volume between the imaged sample and the entire MEA. Nonetheless, local variations throughout the sample can affect effective transport properties, given that transport processes are occurring at and below the resolution captured by the volumes in this work.

Phase and interpenetration thickness.—The values for the layer thickness of the three solid phases, as well as the interpenetration thickness of the MPL into the GDL, are given in Table II. Throughout the nine regions of the sample, the MPL was found to have the greatest variation in thickness, with a deviation of ∼40% around the mean, compared to 12% for the GDL and 20% around the CL. This variation could arise during the manufacturing process, where the MPL is first laid onto the GDL, thus filling pores and penetrating into the GDL. This is evident in the interpenetration thickness of the MPL in the GDL, shown in Table II, where the interpenetration of the MPL and GDL varies between 5% and 11% of the GDL thickness, with the least extent of interpenetration being in region 9 and the greatest extent being in region 2.

Average values for layer thickness throughout the nine regions were found to be 170 μm, 33 μm and 17 μm for GDL, MPL and CL, respectively. These values are in good agreement with those found in other studies,[34,35] but as was previously discussed, these mean values are accompanied with large local variation throughout the nine samples. This is an important consideration both for manufacture of MEAs and for modelling fuel cell performance, as these results show that the layers are inhomogeneous throughout the MEA.

Tortuosity factor of GDL.—The values for the tortuosity factor determined using TauFactor, along with the corresponding values of porosity of the GDL, for the nine regions are shown in Fig. 2b (see
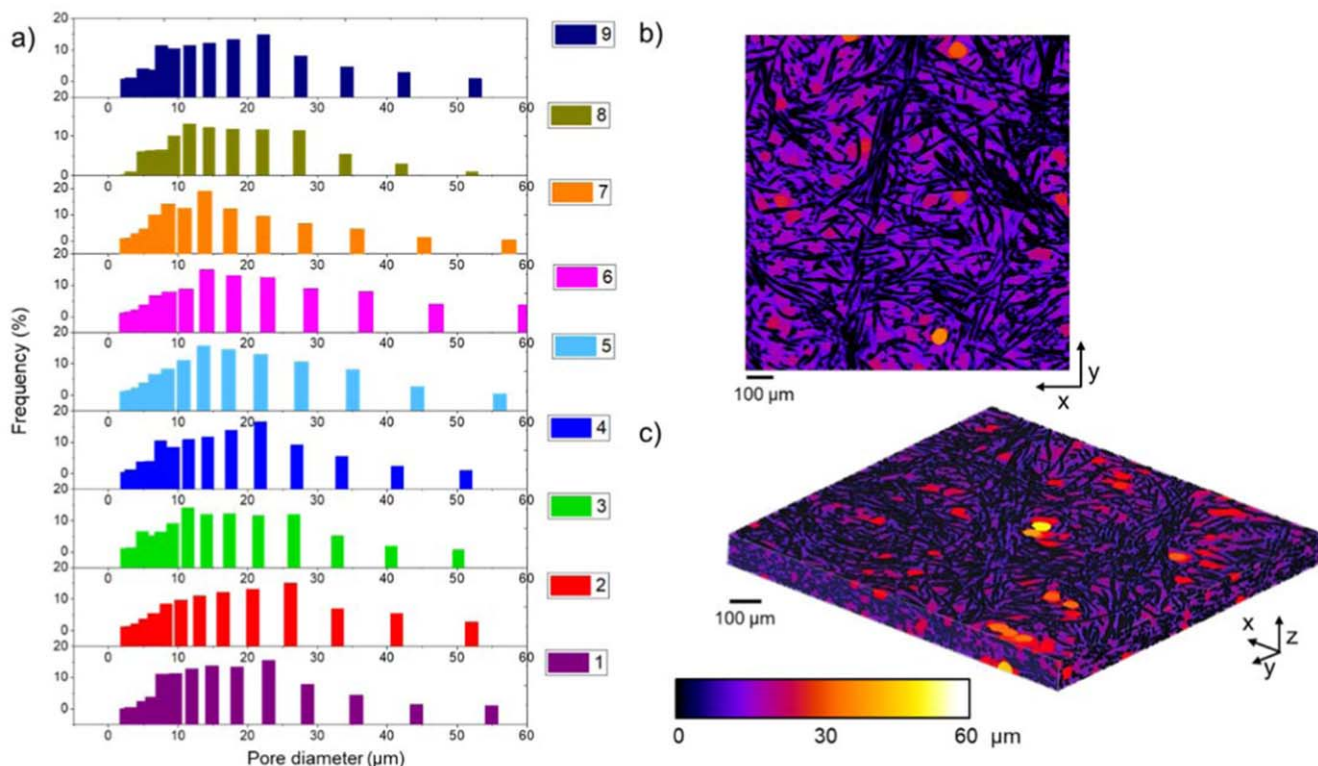
Figure 3. (a) Pore size distribution for the nine regions (1–9, bottom to top), (b) an *xy* slice from region 5 showing local thickness and (c) a volume rendering showing fibres and the isolated pores.

data in Supplementary Information). The results show that the tortuosity factor ranges between 1.63–1.93, which represents a 14% deviation around the mean tortuosity factor of 1.75. Therefore, it is shown that there is stochastic regional variation in the tortuosity factor that doesn't correlate to the region of the sample. Such variations are in agreement with other work.[36] This is further highlighted by the variation in porosity throughout the nine regions (Fig. 2b, blue axis), with porosity values varying between 61.6% and 67.0%. Despite this local variation, previous work has shown that for an ROI of a GDL with similar dimensions (on the order of 1 mm), transport properties reach a representative area.[22]

Thus, the findings here indicate that whilst a 1.2 mm × 1.2 mm subvolume is representative of the sample at that location, it cannot be assumed that the value calculated at one region of interest in the sample is representative throughout the entirety of a 25 cm² GDL. This conclusion is expected to have implications when modelling global fuel cell performance or degradation rates, as will be discussed in later sections of this paper.

Pore size distribution.—The pore size distribution of the pores in the GDL for each region is plotted in Fig. 3a. The results show that there is a wide distribution of pore sizes throughout the GDL. All regions show a similar distribution of pore sizes, with a broad maximum somewhere between 10 μm and 20 μm and a tail-off out to pore diameters of up to 60 μm. The presence of areas with large pore sizes can be clearly seen in the *xy*-orthoslice and 3D rendering (Figs. 3b and 3c, respectively), where the majority of pores are represented by the blue/purple colour, corresponding to pore diameters between 10–30 μm, with regions of yellow indicating localised pores with larger diameters towards 60 μm. In an operating fuel cell, with two-phase flow of gases and water, pore size and wettability have a crucial effect on fuel cell operation. Adequate capillary transport is necessary for avoiding flooding of the GDL, by way of the capillary forces that act to drive out the water from between the fibres,[37–39] so a variation in pore diameter throughout
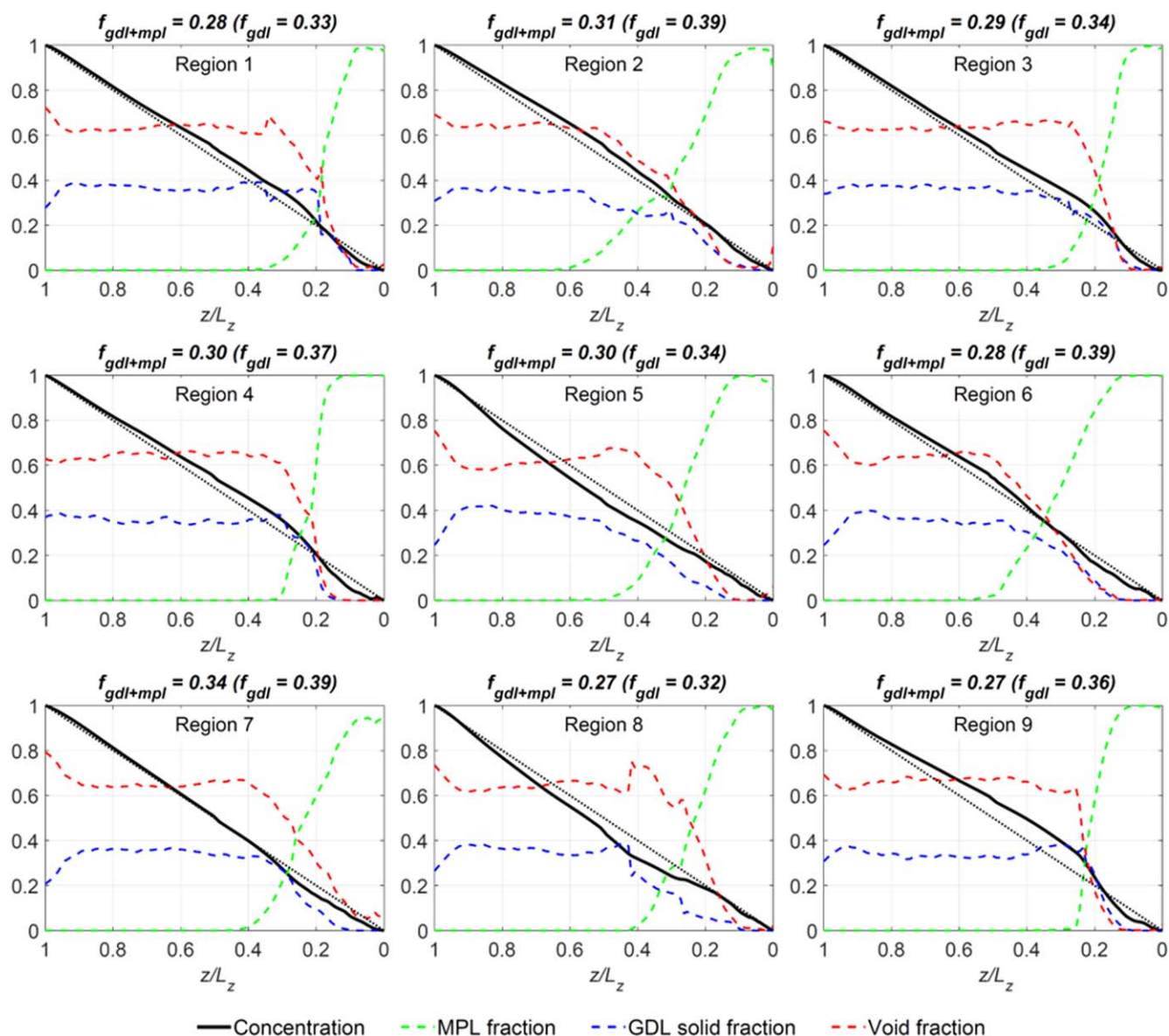
the MEA will result in changes of the local water saturation and gas concentrations.

Mean pore diameters are listed for the samples in Table III. Literature values for the pore diameter of various GDL materials has been found to range between 16 μm–60 μm,[18,39–42] with the range reflecting the fact that the morphology of fibres, and therefore pore sizes, in GDLs from different manufacturers vary. The pore size diameters calculated here for the Freudenberg H23C9 paper are in agreement with those reported for similar Freudenberg papers in the literature,[43,44] with values ranging between 15.1 μm and 21.8 μm. The large standard deviation for all values reflects the fact that there is a large distribution of pore sizes, as is shown in Fig. 3a.

Effective diffusivity.—Modelling of the transport properties was extended from single-phase analysis of the GDL to analysis of multiple phases by including the effect of the MPL on the calculation of effective diffusivity (Fig. 4). In contrast to the values given in Fig. 1c for the total volume fraction for each entire ROI, Fig. 4 shows the local 2D volume fraction of each phase (as shown by the dashed lines) moving slice-by-slice up through the *z*-axis of

Table III. Calculated average pore diameter for each region. The standard deviation is shown in brackets.

Region	Average pore diameter (standard deviation, σ)/μm
1	17.0 (9.3)
2	19.5 (12.6)
3	16.0 (9.1)
4	17.0 (9.4)
5	17.6 (10.6)
6	21.8 (16.2)
7	15.1 (9.6)
8	16.8 (9.9)
9	16.6 (9.6)

Figure 4. Plots of the dimensionless concentration and phase volume fraction (*y*-axis) of regions 1–9, as a function of the *z*-coordinate (as defined in Fig. 1c). The profile corresponding to a linear concentration drop is also shown by a dotted line to guide the reader.

each ROI. The *x*-axis of each graph shows the normalised coordinate of the sample in the *z*-direction, with a value of 0 corresponding to the bottom of the sample, where the primary phase is MPL and a value of 1 corresponding to the top of the GDL. It can, therefore, be seen how the volume fraction of each phase in an orthoslice changes when moving from the bottom to the top of the sample from the MPL, to an MPL/GDL transition region, to the GDL at the top.

As was found for the structural properties, the computed normalised effective diffusivity of the different regions vary stochastically throughout the GDE. The average value was found to be 0.29 ($\sigma=0.02$), with the maximum difference in the effective diffusivity between regions equal to 0.07, giving a relative deviation with respect to the mean of around 6% (see data in Table IV and computed distributions in Supplementary Information). As shown in Fig. 4, the stochastic variations of the effective diffusivity of the GDL + MPL samples arise from the fluctuations of the effective diffusivity of the GDL substrate (see, e.g., the sample-to-sample variations found in[36]), which are in turn impacted by the variations introduced by the MPL. Thus, the microstructure and morphology of the GDL substrate (e.g., pore shape[22]), the GDL-MPL transition region (e.g., the complete or partial penetration of the MPL into

thicker or narrower pores of the GDL) and the MPL (e.g., the presence of cracks) are all factors that affect the overall effective diffusivity. In particular, as shown in Fig. 5, a weak correlation (low R^2 value of 0.327) was found between the ratio of the effective diffusivity of the samples with/without MPL ($f_{gdl+mpl}/f_{gdl}$) and the average MPL volume fraction present in the MPL-coated sample. This shows that the effective diffusivity in regions with thicker MPLs (more MPL material), such as 2 and 6, are in overall terms more affected by the MPL (lower $f_{gdl+mpl}/f_{gdl}$). However, the MPL thickness is not the only contributing factor as can be seen for region 9, which is also notably affected by the addition of the MPL, but has an MPL volume fraction similar to other samples that are less impacted. This highlights the importance of the GDL-MPL transition region, MPL macro- and microstructure (e.g., cracks morphology and connectivity, irregular thickness and penetration depth) in addition to the effects arising from the MPL thickness alone.[45]

Figure 6 shows the limiting current density for $T = 80$ °C, RH = 0.9 and $p_g = 1$ bar, with the GDL-only shown in blue and GDL + MPL shown in green. The mean current density increases from 2.1 A cm^{-2} to 2.7 A cm^{-2} once the MPL has been included.

Table IV. Calculated normalised effective diffusivity, porosity, tortuosity factor, effective diffusivity ratio, and limiting current density corresponding to the samples without MPL and with MPL. The porosity and tortuosity factor are only indicated for the GDL since the MPL is treated as an effective porous medium in this work.

Region	Norm. eff. diffusivity (GDL) f_{gdl}	Porosity (GDL) ε_{gdl}	Tortuosity factor (GDL) τ_{gdl}	Norm. eff. diffusivity (GDL + MPL) $f_{gdl+mpl}$	Ratio $f_{gdl+mpl}/f_{gdl}$	Limiting current density/Acm^{-2} GDL/ GDL + MPL
1	0.332	0.638	1.922	0.276	0.8321	1.841/2.483
2	0.389	0.671	1.726	0.306	0.7885	2.489/2.892
3	0.344	0.646	1.879	0.290	0.8428	2.071/2.770
4	0.375	0.643	1.713	0.304	0.8095	2.194/2.793
5	0.344	0.641	1.864	0.297	0.8637	2.090/2.703
6	0.386	0.654	1.692	0.281	0.7264	2.424/2.677
7	0.39 0	0.664	1.701	0.339	0.8674	2.267/3.088
8	0.324	0.660	2.037	0.270	0.8333	1.804/2.327
9	0.356	0.658	1.849	0.274	0.7704	2.086/2.580
Mean	0.360	0.653	1.820	0.293	0.815	2.141/2.702
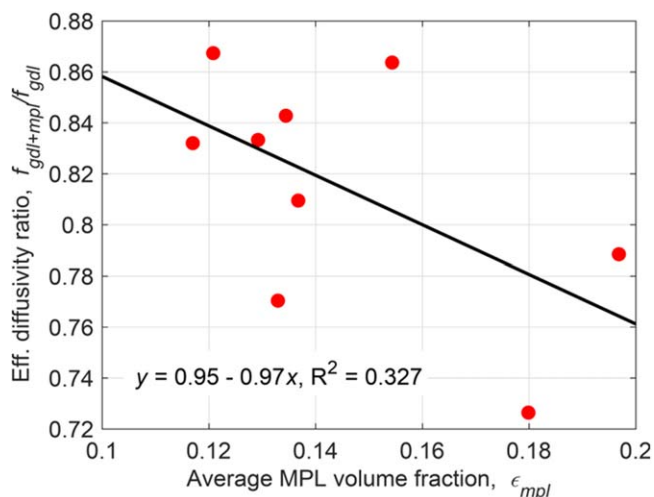
Figure 5. Variation of the effective diffusivity ratio, $f_{gdl+mpl}/f_{gdl}$, as a function of the average MPL volume fraction of regions 1–9. The linear fit to the data points is also included.
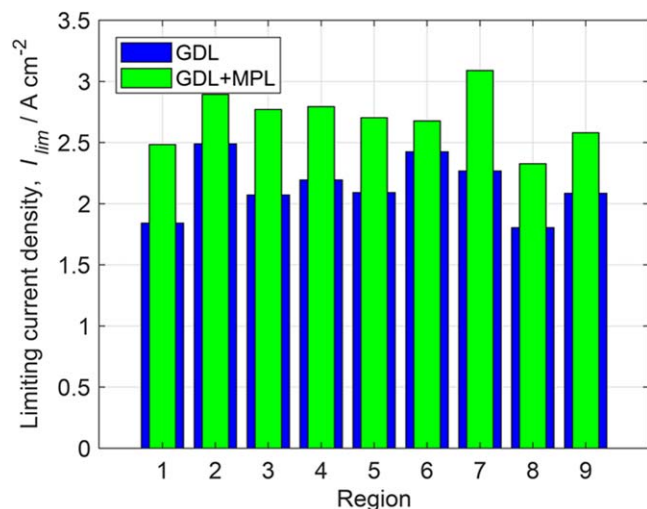
Figure 6. Variation of the limiting current density as a function of the sample location, without MPL (blue) and with MPL (green). Operating conditions: $T = 80\,°C$, $RH = 0.9$ and $p_g = 1$ bar.

The increase of the average current density in the MPL-coated GDL arises from the decrease of the average water saturation, which counteracts the effect of the lower dry effective diffusivity of the MPL ($D_{mpl}^{eff,dry}/D^{bulk} = 0.15$). Accounting for different local saturations would be necessary for a more precise estimation of the local current density. As discussed earlier, the results show a notable variation of the limiting current density throughout the MEA, in both cases due to the stochastic fluctuations of the diffusive transport resistance (mainly effective diffusivity), with the difference between the maximum and minimum current density around 0.7 A cm^{-2}. The homogeneity factor for both the GDL-only and GDL + MPL cases is equal to 0.9. Such variation can be important in terms of fuel cell performance and it is expected that inhomogeneous current distribution will have an effect on local degradation rates. This would be evident in variation in the regional morphology of aged MEAs and will be the subject of future work. Moreover, scalability of layered MEA materials with more homogenous transport properties is an important aspect to be considered in fuel cell manufacturing. For example, GDL fabrics that can suffer from larger heterogeneities (e.g., SIGRACET carbon paper) should be analysed and compared.[18]

In addition, other sources of inhomogeneities, such as the fact that the MEA was not under compression, (the flow fields have been shown to vary the microstructure of the GDL[46]), or the localised accumulation of water, can play a role in performance and durability of an MEA. These factors along with the impact of variable catalyst layer and membrane thickness at higher operating voltages should be further examined experimentally and numerically.

Investigation 2: comparison of region at 4× and 20× magnification.—To analyse whether scans at higher resolutions can be deemed representative of the sample, an internal scan of the central region, region 5, was carried out using 20× optics. Calculation of the volume fraction for each sample shows the values for each solid phase to be higher in all cases for the 20× scan than the 4× scan. Whilst there is only a 1.2% and 0.7% difference for GDL and CL, respectively, the difference in MPL values is 3.9%. The larger difference between MPL volume fractions could arise due to the clearer definition of the MPL in the 20× scan.

To further investigate the effect of resolution, a region of the 4× scan was isolated to exactly match the 20× volume, shown by the dashed red line in Fig. 7a. In this extracted region, the GDL volume fraction is 1.9% larger than the GDL volume fraction in the 20× scan. This shows that there are differences in the segmentation of this phase at the two resolutions, even though the volume of both regions is identical. The MPL volume fraction is 2.8% larger in the cropped 4× subvolume than in the 20× volume, whilst the CL of the cropped 4× regions is only 0.1% smaller than the 20× CL volume fraction (Table V). The findings here show that there are two competing effects: firstly, the resolution of the scan impacts the segmentation, since edges of features are better defined at higher resolutions and, secondly, differences in the size of the volume give different results for each phase since more material is sampled in the 4× scan. Considering this trade-off against the findings in the following section, as well as the previous findings of García-Salaberri et al.,[18] these results indicate that sampling a larger volume is more important for ensuring the scan is representative of the local ROI.

The tortuosity factor of an $a \times b \times 100\ \mu m$ subvolume, where a and b are the xy dimensions of the 4×, cropped 4× and 20× regions, was calculated on the pore phase of the GDL. The tortuosity factor calculated for the 4× scan is 1.79, which is 0.12 higher than the value of the 20× scan. Higher still is the tortuosity factor of the cropped 4× region, with a value of 1.91 (0.38 higher than the 20× sample). The higher value of the cropped 4× sample indicates that the tortuosity factor is dependent on the dimensions of the volume, which is further discussed in the following section.

The average pore diameter of the 20× scan is 18.2 μm ($\sigma = 11.8$), which is slightly larger than the value of 17.6 μm ($\sigma = 10.6$) for the 4× scan. This implies an inverse relationship between average pore diameter and tortuosity factor; larger pores facilitate the transport of species through the GDL. The 4× cropped region has an average pore diameter of 16.29 μm ($\sigma = 9.7$), which could explain the high tortuosity factor of 1.91. Again the variation in results shows competing effects on the volume imaged. At higher resolutions, edges of resolvable features, such as the fibres, are more well defined, which should improve the quality of the segmentation. However, the trade-off comes from the loss of material sampled when using higher resolution scans. The effect of resolution has previously been investigated in detail for solid oxide fuel cell (SOFC) materials by Heenan et al.[47] and Bertei et al.[48] using a fractal analysis method, which could similarly be applied to PEFC materials in future work.

Investigation 3: growing the REA.—The xy dimensions of region 5 were incrementally grown from 10%–100% of the original 1200 $\mu m \times 1200\ \mu m$ dimension, to probe the local representative elementary area. The voxel size remained constant throughout and only the size of the subvolume was altered. Ten regions were selected, with a growth in the xy-direction by a constant factor each time, keeping the z-depth the same for all samples. (Fig. 8a). The
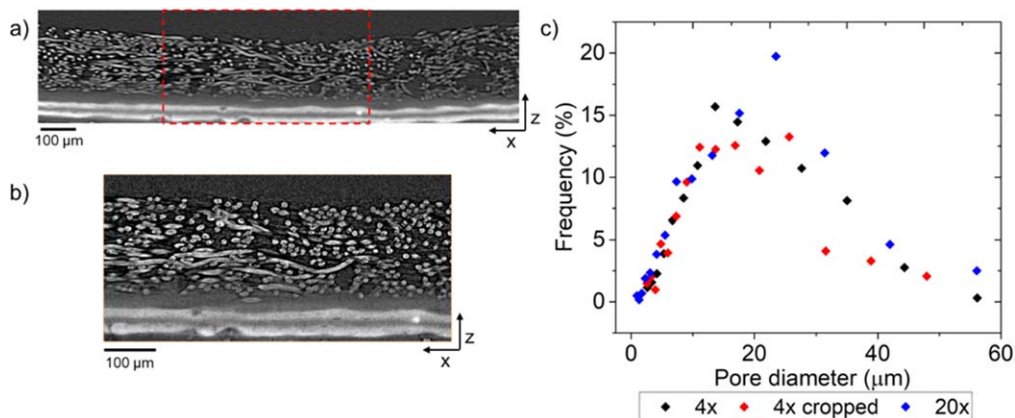
Figure 7. (a) 4× orthoslice and (b) 20× orthoslice. The red dashed box highlights the region of the 4× scan that was cropped to match the 20× scan. (c) pore diameter distribution of 4× (black), 4× cropped (red) and 20× (blue).

Table V. Calculated metrics of interest for the 4× and 20× samples.

Sample	Volume fraction, GDL/%	Volume fraction, MPL/%	Volume fraction, CL/%	Tortuosity factor
4×	17.5	8.6	4.3	1.79
Cropped 4×	20.6	9.7	4.9	1.91
20×	18.7	12.5	5.0	1.53

volume fractions for each phase are shown in Fig. 8b, with closed squares and open diamonds corresponding to the 4× scan and 20× scan, respectively.

For the 20× scan, it can be seen that GDL regions with dimensions greater than 200 μm^2 follow the same trend as that of the 4× sample, with close agreement between the GDL volume fraction values for both the 4× and 20× scans. Similarly, the catalyst layer volume fraction values calculated for the 20× scan are almost identical to those of the 4× scan across all dimensions. However, there is around a 4% difference in MPL volume fractions, even though the values for both 4× and 20× are relatively constant at dimensions greater than 30% of the original. Since it was found in the previous section that the MPL values for the 4× and 20× scans were in poor agreement with each other, the variation is attributed to differences in the segmentation of the samples, arising as a result of the resolution and level of detail achieved by the scan.

The tortuosity factor is plotted as a function of the incremental growth for the 4× and 20× scans in Fig. 8c. For the 4× scan, there is a drop in tortuosity factor of 0.12 between 120 and 240 μm and an increase between 480 and 600 μm of 0.12. At lengths greater than 600 μm, the tortuosity factor becomes more constant, with a difference of 0.06 when the *xy* dimensions are between 600 and

1200 μm. This is a 3% change in the value, which is sufficiently low to suggest that the REA has been reached after this dimension. It should be noted that the REA is considered here, since there is no change in the *z*-dimension. On the other hand, the tortuosity factor for incremental growth of the 20× scan does not appear to have stabilised (Fig. 8c, open diamonds). After an initial increase from 1.36 to 1.69, the tortuosity factor decreases again for regions greater than 200 μm^2, and seems to be levelling off after 300 μm^2, but it cannot be concluded whether it has fully stabilised. This indicates that modelling of transport properties in the GDL when scanning with 20× magnification would not be representative of the local region of interest, since it cannot be said with confidence that the REA has been reached.

Conclusions

Considering the range of length scales characteristic of the membrane electrode assembly (MEA), as well as the trade-off between resolution and field-of-view, this work has investigated the variations in metrics throughout an entire MEA by selecting nine regions of interest. After scanning the regions using X-ray CT and segmentation of the phases of interest, namely carbon fibres of the
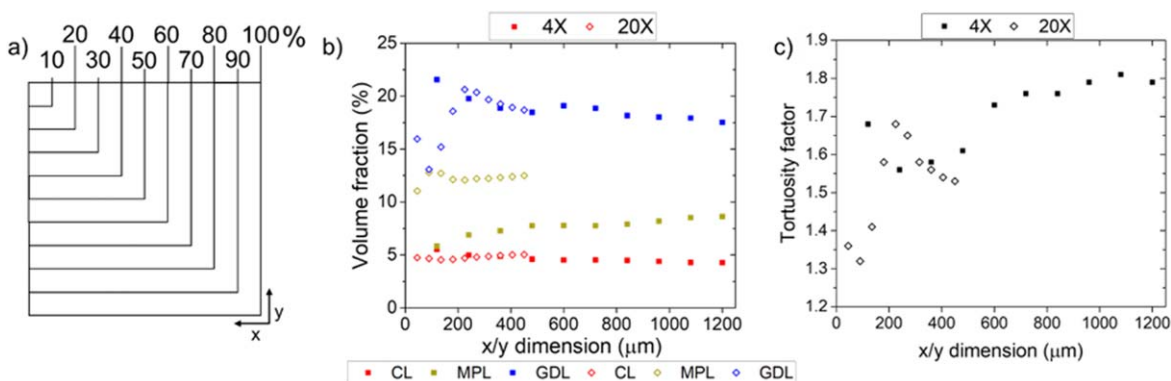
Figure 8. (a) Regions of incremental growth shown as a function of the percentage of the *x*- (or *y*-) width. (b) volume fractions for each phase and (c) tortuosity factor and effective diffusivity in the ten growth regions.

gas diffusion layer (GDL), microporous layer (MPL) and catalyst layer (CL), a number of metrics of interest were calculated from the scans.

Microstructural quantities investigated have included the 3D volume fraction of each phase, the layer and penetration thickness of the various phases in the scan, namely the GDL, MPL and CL. Finally, the tortuosity factor and pore diameters were calculated for an isolated volume of each region containing the GDL phase, only. It was notable that throughout the nine regions, there was stochastic variation in the values calculated. When considering these variations with respect to the fact that each region represented 0.05% of the 25 cm^2 MEA, the differences may appear small. However, the findings do highlight that the GDE is heterogeneous and this variation directly influences the results of the electrochemical modelling.

The heterogeneity was further elucidated by calculation of the effective diffusivity in the MPL and GDL throughout all regions. As with the findings related to the microstructural properties, the values calculated for effective diffusivity varied stochastically in regions throughout the GDE. The values were influenced by both the stochastic fluctuations of the microstructure of the GDL and the MPL. A weak but positive correlation was found between the relative effect of the MPL on gas diffusion and the MPL volume fraction, so regions with a higher MPL volume fraction showed a stronger reduction of the overall effective diffusivity compared to the GDL substrate alone. Electrochemical modelling of the limiting current density, calculated using the effective diffusivity values, confirmed the stochastic nature of the GDE, highlighting that the local performance throughout the MEA can vary notably. Whilst the additional effects of water formation in the pores were not taken into account here, it highlights the need for practitioners to consider local variations when carrying out modelling studies and should be examined further in future experimental and numerical work.

Finally, investigations into the effect of resolution were carried out by:

(a) Comparing a scan of a region imaged with a 4× optic to an identical region scanned using a 20× optic. As a further comparison, the 4× region was cropped, post-segmentation to match the dimensions of the 20× scan.

(b) Growing the 4× and 20× ROIs incrementally from 10%–100% of the original *xy* dimensions, with calculation of solid volume fraction and tortuosity factor for each region.

In both investigations, it was clear that there are two competing effects with the varying resolution: features are better defined at higher resolutions, but this is accompanied by a compromise on the smaller region that is imaged. Results showed that with the 20× optic, a true REA cannot confidently be defined.

It should, however, be emphasised here that although the REA was found to be around 600 μm for the region scanned with 4× optic, the results of Investigation 1 demonstrate that there is significant local variation throughout the nine regions of the MEA. Thus, the findings in this study have shown the need to sample multiple locations of an MEA when using X-ray CT to truly represent the microstructural properties of the MEA as a whole. This has implications for imaged based modelling of fuel cells and is of particular importance when including the effects of compression and localised resistances throughout the active areas, showing that fuel cell modelling cannot be approached as a one-dimensional problem.

Acknowledgments

References

1. E. Maire and P. J. Withers, "Quantitative X-ray tomography." *Int. Mater. Rev.*, **59**, 1 (2014).
2. A. Tkachuk, F. Duewer, H. Cui, M. Feser, S. Wang, and W. Yun, "X-ray computed tomography in Zernike phase contrast mode at 8 keV with 50-nm resolution using Cu rotating anode X-ray source." *Z. Krist.*, **222**, 650 (2007).
3. A. Pokhrel, M. El Hannach, F. P. Orfino, M. Dutta, and E. Kjeang, "Failure analysis of fuel cell electrodes using three-dimensional multi-length scale X-ray computed tomography." *J. Power Sources*, **329**, 330 (2016).
4. M. Fazeli, J. Hinebaugh, Z. Fishman, C. Tötzke, W. Lehnert, I. Manke, and A. Bazylak, "Pore network modeling to explore the effects of compression on multiphase transport in polymer electrolyte membrane fuel cell gas diffusion layers." *J. Power Sources*, **335**, 162 (2016).
5. T. M. M. Heenan, C. Tan, J. Hack, D. J. L. Brett, and P. R. Shearing, "Developments in X-ray tomography characterization for electrochemical devices." *Mater. Today*, **31**, 69 (2019).
6. Q. Meyer et al., "Effect of gas diffusion layer properties on water distribution across air-cooled, open-cathode polymer electrolyte fuel cells: a combined ex-situ X-ray tomography and in-operando neutron imaging study." *Electrochim. Acta*, **211**, 478 (2016).
7. N. Kulkarni, Q. Meyer, J. Hack, R. Jervis, F. Iacoviello, K. Ronaszegi, P. Adcock, P. R. Shearing, and D. J. L. Brett, "Examining the effect of the secondary flow-field on polymer electrolyte fuel cells using X-ray computed radiography and computational modelling." *Int. J. Hydrogen Energy*, **44**, 1139 (2019).
8. R. Jervis, M. D. R. Kok, J. Montagut, J. T. Gostick, D. J. L. Brett, and P. R. Shearing, "X-ray nano computed tomography of electrospun fibrous mats as flow battery electrodes." *Energy Technol.*, **6**, 2488 (2018).
9. Q. Meyer, J. Hack, N. Mansor, F. Iacoviello, J. J. Bailey, P. R. Shearing, and D. J. L. Brett, "Multi-scale imaging of polymer electrolyte fuel cells using X-ray micro- and nano-computed tomography, transmission electron microscopy and helium-ion microscopy." *Fuel Cells*, **19**, 35 (2019).
10. J. Hack, T. M. M. Heenan, F. Iacoviello, N. Mansor, Q. Meyer, P. Shearing, N. Brandon, and D. J. L. Brett, "A structure and durability comparison of membrane electrode assembly fabrication methods: self-assembled vs hot-pressed." *J. Electrochem. Soc.*, **165**, F3045 (2018).
11. Q. Meyer, N. Mansor, F. Iacoviello, P. L. Cullen, R. Jervis, D. Finegan, C. Tan, J. Bailey, P. R. Shearing, and D. J. L. Brett, "Investigation of hot pressed polymer electrolyte fuel cell assemblies via X-ray computed tomography." *Electrochim. Acta*, **242**, 125 (2017).
12. E. F. Medici, I. V. Zenyuk, D. Y. Parkinson, A. Z. Weber, and J. S. Allen, "Understanding water transport in polymer electrolyte fuel cells using coupled continuum and pore-network models." *Fuel Cells.*, **16**, 725 (2016).
13. Y. Singh, F. P. Orfino, M. Dutta, and E. Kjeang, "3D visualization of membrane failures in fuel cells." *J. Power Sources*, **345**, 1 (2017).
14. R. T. White, A. Wu, M. Najm, F. P. Orfino, M. Dutta, and E. Kjeang, "4D in situ visualization of electrode morphology changes during accelerated degradation in fuel cells by X-ray computed tomography." *J. Power Sources*, **350**, 94 (2017).
15. P. A. García-Salaberri, G. Hwang, M. Vera, A. Z. Weber, and J. T. Gostick, "Effective diffusivity in partially-saturated carbon-fiber gas diffusion layers: effect of through-plane saturation distribution." *Int. J. Heat Mass Transf.*, **86**, 319 (2015).
16. J. Hinebaugh, Z. Fishman, and A. Bazylak, "Unstructured pore network modeling with heterogeneous PEMFC GDL porosity distributions." *J. Electrochem. Soc.*, **157**, B1651 (2010).
17. S. Hasanpour, M. Hoorfar, and A. B. Phillion, "Characterization of transport phenomena in porous transport layers using X-ray microtomography." *J. Power Sources*, **353**, 221 (2014).
18. P. A. García-Salaberri, I. V. Zenyuk, A. D. Shum, G. Hwang, M. Vera, A. Z. Weber, and J. T. Gostick, "Analysis of representative elementary volume and through-plane regional characteristics of carbon-fiber papers: diffusivity, permeability and electrical/thermal conductivity." *Int. J. Heat Mass Transf.*, **127**, 687 (2018).
19. S. Bruns, S. L. S. Stipp, and H. O. Sørensen, "Statistical representative elementary volumes of porous media determined using greyscale analysis of 3D tomograms." *Adv. Water Resour.*, **107**, 32 (2017).
20. S. Litster, W. K. Epting, E. A. Wargo, S. R. Kalidindi, and E. C. Kumbur, "Morphological analyses of polymer electrolyte fuel cell electrodes with nano-scale computed tomography imaging." *Fuel Cells.*, **13**, 935 (2013).
21. S. H. Kim and H. Pitsch, "Reconstruction and effective transport properties of the catalyst layer in PEM fuel cells." *J. Electrochem. Soc.*, **156**, B673 (2009).
22. I. V. Zenyuk, D. Y. Parkinson, L. G. Connolly, and A. Z. Weber, "Gas-diffusion-layer structural properties under compression via X-ray tomography." *J. Power Sources*, **328**, 364 (2016).
23. S. J. Cooper, A. Bertei, P. R. Shearing, J. A. Kilner, and N. P. Brandon, "TauFactor: an open-source application for calculating tortuosity factors from tomographic data." *SoftwareX*, **5**, 203 (2016).
24. J. Gostick, Z. Khan, T. Tranter, M. Kok, M. Agnaou, M. Sadeghi, and R. Jervis, "PoreSpy: a python toolkit for quantitative analysis of porous media images." *J. Open Source Softw.*, **4**, 1296 (2019).

25. C. Chan, N. Zamel, X. Li, and J. Shen, "Experimental measurement of effective diffusion coefficient of gas diffusion layer/microporous layer in PEM fuel cells." *Electrochim. Acta*, **65**, 13 (2012).
26. A. K. C. Wong, R. Banerjee, and A. Bazylak, "Tuning MPL intrusion to increase oxygen transport in dry and partially saturated polymer electrolyte membrane fuel cell gas diffusion layers." *J. Electrochem. Soc.*, **166**, F3009 (2019).
27. M. Andisheh-Tadbir, M. El Hannach, E. Kjeang, and M. Bahrami, "An analytical relationship for calculating the effective diffusivity of micro-porous layers." *Int. J. Hydrogen Energy*, **40**, 10242 (2015).
28. P. A. García-Salaberri, D. G. Sánchez, P. Boillat, M. Vera, and K. A. Friedrich, "Hydration and dehydration cycles in polymer electrolyte fuel cells operated with wet anode and dry cathode feed: a neutron imaging and modeling study." *J. Power Sources*, **359**, 634 (2017).
29. K. Jiao and X. Li, "Three-dimensional multiphase modeling of cold start processes in polymer electrolyte membrane fuel cells." *Electrochim. Acta*, **54**, 6876 (2009).
30. J. P. Owejan, T. A. Trabold, and M. M. Mench, "Oxygen transport resistance correlated to liquid water saturation in the gas diffusion layer of PEM fuel cells." *Int. J. Heat Mass Transf.*, **71**, 585 (2014).
31. J. Zhou, S. Shukla, A. Putz, and M. Secanell, "Analysis of the role of the microporous layer in improving polymer electrolyte fuel cell performance." *Electrochim. Acta*, **268**, 366 (2018).
32. F. S. Nanadegani, E. N. Lay, and B. Sunden, "Effects of an MPL on water and thermal management in a PEMFC." *Int. J. Energy Res.*, **43**, 274 (2019).
33. F. C. Cetinbas, R. K. Ahluwalia, A. D. Shum, and I. V. Zenyuk, "Direct simulations of pore-scale water transport through diffusion media." *J. Electrochem. Soc.*, **166**, F3001 (2019).
34. I. V. Zenyuk, P. K. Das, and A. Z. Weber, "Understanding impacts of catalyst-layer thickness on fuel-cell performance via mathematical modeling." *J. Electrochem. Soc.*, **163**, F691 (2016).
35. J. P. Owejan, J. E. Owejan, W. Gu, T. A. Trabold, T. W. Tighe, and M. F. Mathias, "Water transport mechanisms in PEMFC gas diffusion layers." *J. Electrochem. Soc.*, **157**, 1456 (2010).
36. G. S. Hwang and A. Z. Weber, "Effective-diffusivity measurement of partially-saturated fuel-cell gas-diffusion layers." *J. Electrochem. Soc.*, **159**, 683 (2012).
37. A. Bazylak, D. Sinton, Z. S. Liu, and N. Djilali, "Effect of compression on liquid water transport and microstructure of PEMFC gas diffusion layers." *J. Power Sources*, **163**, 784 (2007).
38. J. T. Gostick, M. W. Fowler, M. A. Ioannidis, M. D. Pritzker, Y. M. Volfkovich, and A. Sakars, "Capillary pressure and hydrophilic porosity in gas diffusion layers for polymer electrolyte fuel cells." *J. Power Sources*, **156**, 375 (2006).
39. P. K. Sinha and C. Y. Wang, "Pore-network modeling of liquid water transport in gas diffusion layer of a polymer electrolyte fuel cell." *Electrochim. Acta*, **52**, 7936 (2007).
40. A. El-Kharouf, T. J. Mason, D. J. L. Brett, and B. G. Pollet, "Ex-situ characterisation of gas diffusion layers for proton exchange membrane fuel cells." *J. Power Sources*, **218**, 393 (2012).
41. R. K. Phillips, B. R. Friess, A. D. Hicks, J. Bellerive, and M. Hoorfar, "Ex-situ measurement of properties of gas diffusion layers of PEM fuel cells." *Energy Procedia*, **29**, 486 (2012).
42. J. T. Hinebaugh, "Pore Network Modeling and Synchrotron Imaging of Liquid Water in the Gas Diffusion Layer of Polymer Electrolyte Membrane Fuel Cells." *Ph.D. Thesis*, University of Toronto, Canada (2015), http://hdl.handle.net/1807/69274.
43. M. Göbel, M. Godehardt, and K. Schladitz, "Multi-scale structural analysis of gas diffusion layers." *J. Power Sources*, **355**, 8 (2017).
44. A. Forner-Cuenca, E. E. Penn, A. M. Oliveira, and F. R. Brushett, "Exploring the role of electrode microstructure on the performance of non-aqueous redox flow batteries." *J. Electrochem. Soc.*, **166**, A2230 (2019).
45. O. S. Burheim, G. A. Crymble, R. Bock, N. Hussain, S. Pasupathi, A. Du Plessis, S. Le Roux, F. Seland, H. Su, and B. G. Pollet, "Thermal conductivity in the three layered regions of micro porous layer coated porous transport layers for the PEM fuel cell." *Int. J. Hydrogen Energy*, **40**, 16775 (2015).
46. N. Kulkarni, M. D. R. Kok, R. Jervis, F. Iacoviello, Q. Meyer, P. R. Shearing, and D. J. L. Brett, "The effect of non-uniform compression and flow-field arrangements on membrane electrode assemblies—X-ray computed tomography characterisation and effective parameter determination." *J. Power Sources*, **426**, 97 (2019).
47. T. M. M. Heenan, C. Tan, R. Jervis, X. Lu, D. J. L. Brett, and P. R. Shearing, "Representative resolution analysis for X-ray CT: a solid oxide fuel cell case study." *Chem. Eng. Sci. X.*, **4**, 100043 (2019).
48. A. Bertei, E. Ruiz-Trejo, K. Kareh, V. Yufit, X. Wang, F. Tariq, and N. P. Brandon, "The fractal nature of the three-phase boundary: a heuristic approach to the degradation of nanostructured solid oxide fuel cell anodes." *Nano Energy.*, **38**, 526 (2017).